Monthly Notices
of the
ROYAL ASTRONOMICAL SOCIETY

Mon. Not. R. Astron. Soc. **414,** 2069–2086 (2011) doi:10.1111/j.1365-2966.2011.18520.x

Relativistic expansion of magnetic loops at the self-similar stage – II. Magnetized outflows interacting with the ambient plasma

Hiroyuki R. Takahashi,[1⋆] Eiji Asano[2] and Ryoji Matsumoto[3]

[1]*Center for Computational Astrophysics, National Astronomical Observatory of Japan, 2-21-1, Osawa, Mitaka, Tokyo 181-8588, Japan*
[2]*Kwasan and Hida Observatories, Kyoto University, 17 Ohmine-cho, Kita Kazan, Yamashina-ku, Kyoto 607-8471, Japan*
[3]*Department of Physics, Graduate School of Science, Chiba University, 1-33 Yayoi-cho, Inage-ku, Chiba 263-8522, Japan*

Accepted 2011 February 10. Received 2011 February 9; in original form 2010 June 22

ABSTRACT

We obtained self-similar solutions of relativistically expanding magnetic loops by assuming axisymmetry and a purely radial flow. The stellar rotation and the magnetic fields in the ambient plasma are neglected. We include the Newtonian gravity of the central star. These solutions are extended from those in our previous work by taking into account discontinuities such as the contact discontinuity and the shock. The global plasma flow consists of three regions, the outflowing region, the post-shocked region and the ambient plasma. They are divided by two discontinuities. The solutions are characterized by the radial velocity, which plays a role of the self-similar parameter in our solutions. The shock Lorentz factor gradually increases with radius. It can be approximately represented by the power of radius with the power-law index of 0.25.

We also carried out magnetohydrodynamic (MHD) simulations of the evolution of magnetic loops to study the stability and the generality of our analytical solutions. We used the analytical solutions as the initial condition and the inner boundary conditions. We confirmed that our solutions are stable over the simulation time and that numerical results nicely recover the analytical solutions. We then carried out numerical simulations to study the generality of our solutions by changing the power-law index δ of the ambient plasma density $\rho_0 \propto r^{-\delta}$. We alter the power-law index δ from $\delta \simeq 3.5$ in the analytical solutions. The analytical solutions are used as the initial conditions inside the shock in all simulations. We observed that the shock Lorentz factor increases with time when the power-law index is larger than 3, while it decreases with time when the power-law index is smaller than 3. The shock Lorentz factor Γ_s can be expressed as $\Gamma_s \propto t^{(\delta-3)/2}$ where δ is the power-law index of the ambient plasma. These results are consistent with the analytical studies by Shapiro.

Key words: hydrodynamics – magnetic fields – stars: flare – stars: magnetic fields – stars: neutron.

1 INTRODUCTION

Soft gamma-ray repeaters (SGRs) and anomalous X-ray pulsars (AXPs) are believed to be young neutron stars with strong magnetic fields ($\sim 10^{15}$ G). They are categorized as magnetars (see e.g. Woods & Thompson 2006; Mereghetti 2008, for review). Their rotation period P and its time derivative $\dot{P}$ are $P \sim 10$ s and $\dot{P} \sim 10^{-10}$ s s^{-1}, respectively. A magnetic field strength inferred by assuming the dipole emission from P and $\dot{P}$ is about 10^{15} G. Persistent X-ray emissions with the luminosity of $L_X \sim 10^{34}$–10^{36} erg s^{-1} are observed in SGRs and AXPs. SGRs are identified by the hard X-ray bursts. Extraordinary energetic outbursts called giant flares are observed in three SGRs. The burst energy in the SGR 1806-20 giant flares on 2004 December 27 reached $\sim 10^{47}$ erg (Terasawa et al. 2005). Since SGRs and AXPs are not accretion-powered sources, it is believed that their activity is driven by dissipation of their magnetic fields.

Strong magnetic fields are created by the dynamo mechanism during the core collapse of a supernova progenitor. At this stage, the star becomes unstable against the convective mode since the entropy gradient becomes negative, ($dS/dr < 0$) due to the neutrino cooling (Burrows 1987; Keil, Janka & Mueller 1996). Thus, the infant neutron star can store a large amount of magnetic energies. The magnetic fields are also amplified after the birth of the magnetar. The interior of the star rotates differentially at its birth when the equation of state

⋆E-mail: takahashi@cfca.jp

is stiff. The internal magnetic fields can be amplified up to 10^{17} G due to the dynamo mechanisms (Duncan & Thompson 1992). As the magnetic helicity is accumulated inside the star, the Lorentz force exerted by the twisted magnetic fields balances with the rigidity of the crusts. When the critical twists are accumulated, the crustal rigidity can no longer sustain the Lorentz force by the strong magnetic fields. The magnetic helicity is then injected into the magnetosphere. The resulting crustal motion induces the electric fields and it results in creating the potential difference between the foot-points of the magnetic loops. The particles injected from the interior of the star are accelerated along the magnetic field lines due to the potential difference. The accelerated particles initiate the avalanches of the pair creation (Beloborodov & Thompson 2007). These particles carry the electric current, which twists the global magnetic fields. When the dynamical equilibrium is lost by the accumulated magnetic twists, the magnetic loops expand by the magnetic pressure gradient force. Inside the magnetic loops, a current sheet similar to that of solar flares is formed. The magnetic reconnections taking place in the current sheet are responsible for the magnetic energy release and resulting flares (Lyutikov 2006). Recent observations which indicate the topological change of the global magnetic fields before and after the giant flares support these models (Woods et al. 2001).

Motivated by the magnetar flare model, Spitkovsky (2005) performed two-dimensional relativistic force-free simulations of magnetar flares by injecting the magnetic twists into the magnetosphere. They showed that the initially dipole magnetic fields are twisted by the foot-point motion, and the loop magnetic fields then expand due to the magnetic pressure gradient force. Asano (2007) carried out two-dimensional relativistic force-free simulations of expanding magnetic loops and showed that the Lorentz factor defined by the drift velocity $\boldsymbol{v}_{\rm d} = c(\boldsymbol{E} \times \boldsymbol{B})/B^2$ exceeds 10 (see Uchida 1997, for the definition of the drift velocity). These simulations indicate that the magnetic loops expand self-similarly.

Such self-similar solutions have been found in analytical studies. In the framework of the force-free dynamics, Lyutikov & Blandford (2003) obtained self-similar solutions of the spherically expanding magnetic shell. Prendergast (2005) found self-similar solutions of the relativistic force-free field in two dimensions. Gourgouliatos & Lynden-Bell (2008) derived relativistic self-similar force-free solutions and analysed them in detail. In the framework of the relativistic magnetohydrodynamics (MHD), Lyutikov (2002) found self-similar solutions of the spherically expanding magnetic shells. Recently, Takahashi et al. (2009) obtained self-similar solutions of magnetic loops (not shell) by extending the non-relativistic solutions obtained by Low (1982b). Gourgouliatos & Vlahakis (2010) obtained solutions by ignoring the gravity from the central star. These authors studied outflows of the magnetized plasma lifted up from the central star. However, they did not consider the interaction between the outflow and the interstellar matter. Low (1984a) obtained non-relativistic self-similar solutions of the expanding magnetic loops interacting with the interstellar matter. In their models, the outflows and the ambient plasma are divided by a contact discontinuity. The forward-propagating wave forms another discontinuity (shock). This solution is useful to understand the coronal mass ejections in solar flares. Stone et al. (1992) employed this solution as a test problem to check the validity and accuracy of axisymmetric MHD codes.

In this paper, we extend the analytic solutions given by Takahashi et al. (2009) by including the contact discontinuity and the shock by extending the non-relativistic model by Low (1984a) to the relativistic regime.

This paper is organized as follows. In Section 2, we summarize the basic equations of self-similar relativistic MHD equations given by Takahashi et al. (2009). In Section 3, we show the solutions of these equations including the two discontinuities. These solutions represent the relativistic coronal mass ejection from the central star. Such solutions are expected to explain the giant flares in magnetars. The physical properties of the solutions are shown in Section 4. We also carried out the two-dimensional relativistic MHD simulations to study the stability of the solutions. The analytical solutions shown in Section 3 are used as the initial and boundary conditions for simulations. These results are shown in Section 5. We summarize our results in Section 6.

2 BASIC EQUATIONS OF SELF-SIMILAR RELATIVISTIC MHD

In the following, we take the light speed as unity. The complete set of the relativistic ideal MHD equations is

$$\frac{\partial}{\partial t}(\gamma\rho) + \nabla\cdot(\gamma\rho\boldsymbol{v}) = 0, \tag{1}$$

$$\rho\gamma\left[\frac{\partial}{\partial t} + (\boldsymbol{v}\cdot\nabla)\right](h\gamma\boldsymbol{v}) = -\nabla p + \rho_e\boldsymbol{E} + \boldsymbol{j}\times\boldsymbol{B} - \frac{GM\rho h\gamma^2}{r^2}\boldsymbol{e}_{\rm r}, \tag{2}$$

$$\left[\frac{\partial}{\partial t} + (\boldsymbol{v}\cdot\nabla)\right]\left(\ln\frac{p}{\rho^{\Gamma}}\right) = 0, \tag{3}$$

$$\nabla\cdot\boldsymbol{E} = 4\pi\rho_e, \tag{4}$$

$$\nabla\cdot\boldsymbol{B} = 0, \tag{5}$$

$$\frac{\partial\boldsymbol{B}}{\partial t} + \nabla\times\boldsymbol{E} = 0, \tag{6}$$

$$\frac{\partial\boldsymbol{E}}{\partial t} = \nabla\times\boldsymbol{B} - 4\pi\boldsymbol{j}, \tag{7}$$

$$\boldsymbol{E} = -\boldsymbol{v} \times \boldsymbol{B}, \tag{8}$$

where $\boldsymbol{E}$, $\boldsymbol{B}$, $\boldsymbol{j}$, $\boldsymbol{v}$, γ, ρ_e, ρ, p and Γ are the electric field, the magnetic field, the current density, the velocity, the Lorentz factor, the charge density, the mass density, the pressure and the specific heat ratio, respectively. The vector $\boldsymbol{e}_{\rm r}$ is a unit vector in the radial direction. Newtonian gravity of the central star is included as an external force. Here, G is the gravitational constant, and r is the distance from the centre of the star. We replaced the gravitational force $-GM\rho\gamma/r^2$ in Takahashi et al. (2009) with $-GM\rho h\gamma^2/r^2$, which can treat the gravitational force of the relativistic plasma more properly (Gourgouliatos & Vlahakis 2010).

The relativistic specific enthalpy including the rest mass energy h is written as

$$h = \frac{\epsilon + p}{\rho} = 1 + \frac{\Gamma}{\Gamma - 1}\frac{p}{\rho} \equiv 1 + h_N, \tag{9}$$

where ϵ is the energy density of the matter including the photon energy coupled with the plasma, and $h_N = \Gamma p/[(\Gamma - 1)\rho]$ is the non-relativistic specific thermal enthalpy.

In the following, we take $\Gamma = 4/3$ which corresponds to the relativistic radiation pressure dominant plasma. Thus, we can study the evolution of a fireball confined by magnetic fields.

We ignore the stellar rotation and assume a purely radial flow. We also assume axisymmetry. The magnetic fields in spherical coordinates (r, θ, ϕ) are then expressed in terms of two independent scalar functions $\tilde{A}$ and B as

$$\boldsymbol{B} = \frac{1}{r\sin\theta}\left(\frac{1}{r}\frac{\partial\tilde{A}}{\partial\theta}, -\frac{\partial\tilde{A}}{\partial r}, B\right). \tag{10}$$

In the following, we assume that the evolution of the magnetic loops can be described by a Lagrangian coordinate η:

$$\eta \equiv \frac{r}{Z(t)}, \tag{11}$$

where $Z(t)$ is a scale function of time. We further assume that the flux function $\tilde{A}$ evolves with time t and radial distance r through the Lagrangian coordinate η, as

$$\tilde{A}(t, r, \theta) = \tilde{A}(\eta, \theta). \tag{12}$$

The MHD equations are then written as

$$\frac{{\rm d}^2 Z(t)}{{\rm d}t^2} = 0, \tag{13}$$

$$v_{\rm r} = \dot{Z}(t)\eta, \tag{14}$$

$$p(t, r, \theta) = \frac{P(\eta, \theta)}{Z^4(t)}, \tag{15}$$

$$\rho(t, r, \theta)\gamma = \frac{D(\eta, \theta)}{Z^3(t)}, \tag{16}$$

$$B(t, r, \theta) = \frac{Q(\eta, \theta)}{Z(t)}, \tag{17}$$

$$\frac{4\gamma^2 v_{\rm r}^2 P}{\eta} = \frac{\partial P}{\partial\eta} + \frac{1}{4\pi\eta^2\sin^2\theta}\left\{\frac{\partial\tilde{A}}{\partial\eta}\left[\hat{\mathcal{L}}_{(\eta,\theta)}\tilde{A} - \frac{\partial}{\partial\eta}\left(\dot{Z}^2\eta^2\frac{\partial\tilde{A}}{\partial\eta}\right)\right] + Q\frac{\partial}{\partial\eta}\left(\frac{Q}{\gamma^2}\right)\right\} + \frac{GMD\gamma}{\eta^2}\left(1 + \frac{4\gamma P}{ZD}\right) \tag{18}$$

$$\frac{1}{\gamma^2}\frac{\partial\tilde{A}}{\partial\eta}\frac{\partial Q}{\partial\theta} - \frac{\partial\tilde{A}}{\partial\theta}\frac{\partial}{\partial\eta}\left(\frac{Q}{\gamma^2}\right) = 0, \tag{19}$$

$$4\pi\eta^2\sin^2\theta\frac{\partial P}{\partial\theta} + \frac{\partial\tilde{A}}{\partial\theta}\left[\hat{\mathcal{L}}_{(\eta,\theta)}\tilde{A} - \frac{\partial}{\partial\eta}\left(\dot{Z}^2\eta^2\frac{\partial\tilde{A}}{\partial\eta}\right)\right] + \frac{Q}{\gamma^2}\frac{\partial Q}{\partial\theta} = 0, \tag{20}$$

where $\hat{\mathcal{L}}_{(\eta,\theta)}$ is an operator

$$\hat{\mathcal{L}}_{(\eta,\theta)} \equiv \frac{\partial^2}{\partial\eta^2} + \frac{\sin\theta}{\eta^2}\frac{\partial}{\partial\theta}\left(\frac{1}{\sin\theta}\frac{\partial}{\partial\theta}\right) \tag{21}$$

(see Takahashi et al. 2009, for derivation). We can readily solve equation (13) as

$$Z(t) = \sqrt{\xi}t, \tag{22}$$

where ξ is a constant of integral. The radial velocity is obtained from equation (14) as

$$v_{\rm r} = \sqrt{\xi}\eta. \tag{23}$$

By substituting equation (22) into equation (19), we obtain the function Q which has a form

$$Q(\eta, \theta) = \frac{g(\tilde{A})}{1-\eta^2}, \tag{24}$$

where $g(\tilde{A})$ is an arbitrary function of $\tilde{A}$.

We note that the last term in equation (18) includes $Z(t) = \sqrt{\xi}t$, which is a function of time. Thus, this term does not admit the existence of the self-similar solutions because the thermal enthalpy in the gravity term explicitly depends on time. This violation of the self-similarity comes from the difference of the scaling law between the density and the pressure (equations 15 and 16, also see Gourgouliatos & Vlahakis 2010). However, when the contribution of the thermal enthalpy on the gravity is sufficiently small, we can obtain self-similar solutions of the relativistic expansion. The ratio of the gravity for the thermal enthalpy to the plasma inertia is written as

$$\frac{\text{gravity for the thermal enthalpy}}{\text{plasma inertia}} = \frac{|GM\rho h_N \gamma^2/r^2|}{|\rho\gamma D(\gamma h v)/Dt|} = \frac{r_{\rm g}}{rv^2}, \tag{25}$$

where $r_{\rm g} = GM$ is the gravitational radius. Thus, when $r \gg r_{\rm g}$, the gravitational force for the thermal enthalpy h_N is negligible when $v \sim 1$. In this paper, we consider the evolution of the relativistically expanding plasma at large distance where the gravity for the thermal enthalpy $-GM\rho h_N\gamma^2/r^2$ can be neglected. In such region, the plasma inertia is sustained by the pressure gradient and Lorentz forces. When $r \ll R_{\rm s}$, we assume that the rest mass energy density much exceeds the thermal energy density (i.e. $h_N \ll 1$). In this regime, the gravity is expressed as $-GM\rho\gamma^2/r^2$. The Lagrangian coordinate η (see equation 11) then behaves as the self-similar parameter.

Without loss of generality, we can change independent variables of P from (η, θ) to $(\eta, \tilde{A})$ as

$$P(\eta, \theta) = P(\eta, \tilde{A}). \tag{26}$$

By neglecting the thermal enthalpy in the gravitational force $-GM\rho h\gamma^2/r^2$, equations (20) and (18) reduce to the self-similar equations as

$$\frac{\partial P}{\partial \tilde{A}} = -\frac{1}{4\pi\eta^2\sin^2\theta}\left[\hat{\mathcal{L}}_{(\eta,\theta)}\tilde{A} - \frac{\partial}{\partial\eta}\left(\xi\eta^2\frac{\partial\tilde{A}}{\partial\eta}\right) + \frac{g(\tilde{A})}{1-\xi\eta^2}\frac{{\rm d}g(\tilde{A})}{{\rm d}\tilde{A}}\right], \tag{27}$$

$$D = \frac{\eta^2\sqrt{1-\xi\eta^2}}{GM}\left(\frac{4\xi\eta P}{1-\xi\eta^2} - \left.\frac{\partial P}{\partial\eta}\right|_{\tilde{A}}\right). \tag{28}$$

Equations (24), (27) and (28) are the set of the self-similar MHD equations. The explicit solutions can be constructed as follows. First we prescribe an arbitrary function $\tilde{A}(\eta, \theta)$ and the function $g(\tilde{A})$. The pressure function P is determined from equation (27) and the density function D is obtained from equation (28).

Before presenting the solutions of the self-similar MHD equations, we have to note that the self-similar relativistic ideal MHD equations describe the free expansion of the magnetized plasma. By taking time derivative of $\boldsymbol{v}$, we obtain

$$\frac{D\boldsymbol{v}}{Dt} = 0, \tag{29}$$

where we used equations (11), (22) and (23). The plasma is neither accelerated nor decelerated, but it expands with the inertial speed keeping the force balance (this can be confirmed by inserting equation 23 into equation 2, or, see equation 36 in Takahashi et al. 2009).

3 RELATIVISTIC CORONAL MASS EJECTION

In the previous section, we showed the set of the self-similar relativistic MHD equations, which describes the plasma expanding with the inertial speed. In this section, we obtain solutions of these equations by imposing appropriate boundary conditions.

We adopt the simple model of magnetic explosions according to Low models (Low 1984a, see fig. 1). Equations (27) and (28) describe magnetized plasma outflowing from the central star (outflow region). The outflow sweeps up an ambient plasma while it expands. A contact surface would be formed which separates the outflowing plasma with the swept-up ambient plasma. The contact surface is situated at $r = R_{\rm c}(t)$. Ahead of the contact surface, a forward wave propagating into an undisturbed ambient plasma forms a shock at $r = R_{\rm s}(t)$. The swept-up ambient plasma is accumulated in the region in $R_{\rm c}(t) \leqq r \leqq R_{\rm s}(t)$ (post-shock region).

First, we consider the outflow region where the magnetized plasma is lifted up from the central star. Various models of the magnetic field configurations have been proposed (Low 1982b, 1984a; Takahashi et al. 2009). In this paper, we utilize the following flux function (Low 1984a)

$$\tilde{A} = A_0\left[H_0 + \sqrt{\frac{2}{\pi}}\left(\frac{\sin(\lambda\eta)}{\lambda\eta} - \cos(\lambda\eta)\right)\right]\sin^2\theta \equiv A_0 f(\lambda\eta)\sin^2\theta, \tag{30}$$

where

$$f(x) = H_0 + \sqrt{\frac{2}{\pi}}\left(\frac{\sin x}{x} - \cos x\right). \tag{31}$$

Here A_0, H_0 and λ are constants. The flux function given by equation (30) has local maxima (see fig. 4 in Low 1984a). The maximum corresponds to the centre of the flux ropes. This function can thus describe the coronal mass ejection from the central star. Such relativistic

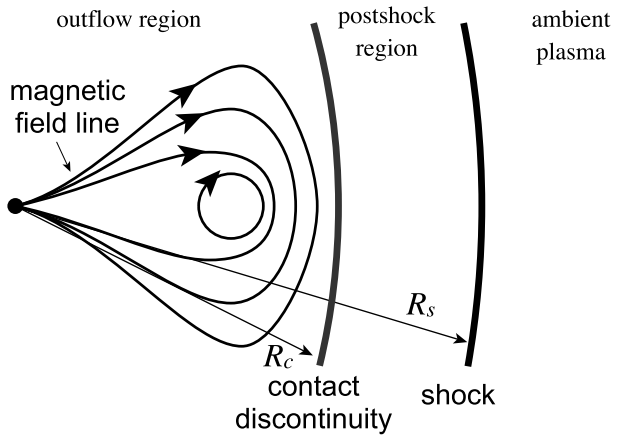

Figure 1. Schematic picture of our models of the relativistic coronal mass ejection. Ahead of the global magnetic loops, two discontinuities exist at $r = R_c(t)$ (contact discontinuity) and $r = R_s(t)$ (shock).

coronal mass ejections can be applied to giant flares in magnetars (Lyutikov 2006). We express the toroidal magnetic field g as a power series of $\tilde{A}$:

$$g(\tilde{A}) = \sum_n \alpha_n \tilde{A}^n, \tag{32}$$

where α_n are constants. Note that the dependence of the toroidal magnetic field on the polar angle is represented by $\sum_n \sin^{2n-1}\theta$ from equations (10), (17), (30) and (32). This indicates that the power-law index n and α_n can be interpreted as the Fourier modes of the toroidal magnetic fields in polar direction and their amplitudes, respectively. The modes and the amplitudes are determined by the boundary condition at which the magnetic shear is injected into the magnetosphere. The shear injection begins before the self-similar expansion starts. In this paper, we do not consider the details of the shear injection from the central star and leave them as free parameters since we consider the self-similar stage.

The explicit forms of the magnetic fields are then written as

$$B_r(t, r, \theta) = \frac{2A_0}{r^2}\left\{H_0 + \sqrt{\frac{2}{\pi}}\left[\frac{\sin(\lambda\eta)}{\lambda\eta} - \cos(\lambda\eta)\right]\right\}\cos\theta, \tag{33}$$

$$B_\theta(t, r, \theta) = -\frac{A_0}{r^2}\sqrt{\frac{2}{\pi}}\left[\cos(\lambda\eta) - \frac{1-(\lambda\eta)^2}{\lambda\eta}\sin(\lambda\eta)\right]\sin\theta, \tag{34}$$

$$B_\phi(t, r, \theta) = \frac{1}{r^2\sin\theta}\frac{\eta}{1-\xi\eta^2}\sum_n \alpha_n \tilde{A}^n. \tag{35}$$

The pressure function of the outflowing plasma P_o is obtained by inserting equations (30) and (32) into equation (27) as

$$P_o(\eta, \theta) = P_A(\eta, \theta) + P_Q(\eta, \theta) + P_i(\eta), \tag{36}$$

where

$$P_A(\eta, \theta) = \frac{A_0\tilde{A}(\eta, \theta)}{4\pi\eta^4}\left\{2H_0 + \sqrt{\frac{2}{\pi}}(\lambda\eta)\left[(1+\xi\eta^2)\sin(\lambda\eta) - (\lambda\eta)(1-\xi\eta^2)\cos(\lambda\eta)\right]\right\}, \tag{37}$$

$$P_Q(\eta, \theta) = -\frac{1}{4\pi\eta^2(1-\xi\eta^2)}\left\{\sum_{m+n\neq 1}\frac{m\alpha_m\alpha_n A_0^{m+n}}{m+n-1}f^{m+n}(\lambda\eta)\sin^{2(m+n-1)}\theta + \sum_{m+n=1} m\alpha_m\alpha_n A_0 f(\lambda\eta)\ln\tilde{A}(\eta, \theta)\right\}. \tag{38}$$

Here P_i arises from the integration. By substituting equations (36)–(38) into equation (28), the corresponding density function D_o is expressed as

$$D_o(\eta, \theta) = D_A(\eta, \theta) + D_Q(\eta, \theta) + D_i(\eta), \tag{39}$$

$$D_A(\eta, \theta) = \frac{A_0\tilde{A}(\eta, \theta)}{4\pi G M\eta^3\sqrt{1-\xi\eta^2}}\Xi(\eta), \tag{40}$$

$$D_Q(\eta,\theta) = -\frac{(3-\xi\eta^2)f(\lambda\eta) - (1-\xi\eta^2)\left[H_0 + \sqrt{\frac{2}{\pi}}(\lambda\eta)\sin(\lambda\eta)\right]}{4\pi GM\eta(1-\xi\eta^2)^{\frac{3}{2}}} \begin{cases} \displaystyle\sum_{m+n\neq 1} \frac{m\alpha_m\alpha_n A_0 \tilde{A}^{m+n-1}(\eta,\theta)}{m+n-1}, & \text{for } m+n\neq 1, \\ \displaystyle\sum_{m+n=1} m\alpha_m\alpha_n A_0 \ln\tilde{A}(\eta,\theta), & \text{for } m+n=1, \end{cases} \tag{41}$$

where the function $\Xi(\eta)$ is defined as

$$\Xi(\eta) = 8H_0 + \sqrt{\frac{2}{\pi}}\lambda\eta\left\{\left[(3-(\lambda\eta)^2)(1+(\xi\eta^2)^2) + 2\xi\eta^2(1+(\lambda\eta)^2)\right]\sin(\lambda\eta) - \lambda\eta(1-\xi\eta^2)(3+5\xi\eta^2)\cos(\lambda\eta)\right\}. \tag{42}$$

The function $D_i(\eta)$ describes the isotropic distribution of the plasma which is related with $P_i(\eta)$ through equation (28).

To determine functions P_i and D_i, we need one more relation between them. We assume that there is no energy/mass injection from the central star at this stage. Since the contact surface separates the outflow region from the post-shock region, the outflow plasma expands adiabatically. We then obtain another relation between $P_i(\eta)$ and $D_i(\eta)$ from the entropy conservation equation as

$$\frac{p_i}{\rho_i^{\frac{4}{3}}} = \text{const} = \frac{\nu}{4}, \tag{43}$$

where $p_i = Z(t)^4 P_i$, $\rho_i = Z(t)^3 D_i$ and ν is a constant. Substituting equations (15), (16) and (23) into equation (43), we obtain

$$P_i = \frac{\nu}{4}\left(1-\xi\eta^2\right)^{\frac{2}{3}} D_i^{\frac{4}{3}}. \tag{44}$$

Substituting equation (44) into (28), we obtain the solutions

$$P_i(\eta) = \frac{1}{4\nu^3}\left(\frac{GM}{\eta} - \frac{\mu}{\sqrt{1-\xi\eta^2}}\right)^4, \tag{45}$$

$$D_i(\eta) = \frac{1}{\nu^3}\frac{1}{\sqrt{1-\xi\eta^2}}\left(\frac{GM}{\eta} - \frac{\mu}{\sqrt{1-\xi\eta^2}}\right)^3, \tag{46}$$

where μ is a constant of integral. These solutions describe the isotropic outflowing plasma in the outflow region.

Next, we consider the post-shock region ($R_c \leqq r \leqq R_s$). The shocked plasma also moves in radial direction. We assume that the shocked plasma evolves self-similarly and obeys the same set of self-similar equations in the outflow region. Then the contact surface moves in radial direction with a constant speed and the radius of the contact surface R_c is expressed as

$$R_c(t) = \eta_c\sqrt{\xi}t, \tag{47}$$

where η_c is a constant. We assumed that the magnetic fields in the ambient plasma can be neglected. From these assumptions, the shocked plasma obeys equation (28). We need another relation between the shocked gas pressure P_s and the shocked gas density D_s. Note that we cannot use the adiabatic relation because the ambient plasma flows into the post-shock region from the shock surface at $r = R_s$. The forward shock compresses and heats up the plasma, resulting in an increase in the entropy. Thus, the entropy in the shocked plasma should be determined by the shock condition at $r = R_s(t)$. Rather than evaluating the entropy variation by the shock, we consider the jump conditions of the plasma density, the pressure and the velocity. The entropy variation is determined after imposing the Rankin–Hugoniot relations between the undisturbed and shocked plasma (Low 1984b).

By assuming the strong shocks, the relativistic Rankin–Hugoniot relations are written as

$$p|_{r=R_s} = \left.\frac{2}{3}\Gamma_s^2\rho_0\right|_{r=R_s}, \tag{48}$$

$$\rho\gamma|_{r=R_s} = \left.2\Gamma_s^2\rho_0\right|_{r=R_s}, \tag{49}$$

$$\gamma^2\big|_{r=R_s} = \frac{1}{2}\Gamma_s^2, \tag{50}$$

with an accuracy of $\mathcal{O}\left(1/\gamma^2\right)$ (Blandford & McKee 1976; Kennel & Coroniti 1984). Γ_s and ρ_0 are the shock Lorentz factor and the plasma mass density of the undisturbed ambient plasma, respectively. Here, we ignore the thermal pressure in the undisturbed plasma by assuming the strong shock.

From equations (23) and (50), we obtain the time evolution of the shock radius as

$$R_s(t) = \frac{3R_0 x_s}{\left(x_s + \sqrt{1+x_s^2}\right)^{\sqrt{2}}\left(\sqrt{2}x_s - \sqrt{1+x_s^2}\right)^2}, \tag{51}$$

where $x_s \equiv R_s/t$ and R_0 is a constant of integral. Combining equations (48) and (49), we obtain the relation between the P_s and D_s:

$$P_s(\eta) = \frac{\sqrt{\xi}R_0}{\left(\sqrt{\xi}\eta + \sqrt{1+\xi\eta^2}\right)^{\sqrt{2}}\left(\sqrt{2\xi}\eta - \sqrt{1+\xi\eta^2}\right)^2} D_s(\eta). \tag{52}$$

Here we use equations (15), (16), (51). Substituting equation (52) into equation (28), P_s and D_s are expressed as

$$P_s = \frac{P_0}{\left(1-\xi\eta^2\right)^2} K\left(\sqrt{\xi}\eta\right), \tag{53}$$

$$D_s = \frac{P_0}{\sqrt{\xi}R_0} \frac{\left(\sqrt{\xi}\eta+\sqrt{1+\xi\eta^2}\right)^{\sqrt{2}}}{\left(\sqrt{2\xi}\eta+\sqrt{1+\xi\eta^2}\right)^2} K\left(\sqrt{\xi}\eta\right), \tag{54}$$

where P_0 is a constant of integral. The function K is expressed as

$$K\left(\sqrt{\xi}\eta\right) \equiv \exp\left[-\frac{GM}{R_0}\int_{\sqrt{\xi}\eta_c}^{\sqrt{\xi}\eta} \mathrm{d}x \frac{\left(x+\sqrt{1+x^2}\right)^{\sqrt{2}}(1-x^2)^{\frac{3}{2}}}{x^2\left(\sqrt{2}x+\sqrt{1+x^2}\right)}\right]. \tag{55}$$

The ambient plasma density is obtained by substituting equations (51) and (54) into (49) as

$$\rho_0(r) = \frac{3P_0}{4r^4}\frac{\eta_0^4}{(1-\xi\eta_0^2)} K\left(\sqrt{\xi}\eta_0\right). \tag{56}$$

Here η_0 should be determined from the following equation:

$$r = \frac{3R_0\sqrt{\xi}\eta_0}{\left(\sqrt{\xi}\eta_0+\sqrt{1+\xi\eta_0^2}\right)^{\sqrt{2}}\left(\sqrt{2\xi}\eta_0-\sqrt{1+\xi\eta_0^2}\right)^2}. \tag{57}$$

Note that the radial profile of the ambient plasma density is not arbitrary but determined by equation (56). Some authors derive the self-similar solutions by prescribing the density profile of the ambient plasma as $\rho_0 \propto r^{-\delta}$, where δ is a constant (Blandford & McKee 1976; Sari 2006). In our approach, we first prescribe the self-similar variables given in equation (11). Then, the outflow velocity is obtained by equation (14). The ambient plasma density is determined by applying the Rankin–Hugoniot relations at the shock. Thus, the ambient plasma density cannot have an arbitrary form, but it is uniquely determined.

Finally, we apply the boundary conditions at $r = R_c$. Since we assumed unmagnetized ambient plasma, the magnetic fields should vanish at $r = R_c$. This condition can determine the parameters H_0 and λ in equation (30). The conditions that $B_r(r = R_c) = 0$ and $B_\phi(r = R_c) = 0$ are expressed as

$$H_0 = -\sqrt{\frac{2}{\pi}}\left(\frac{\sin(\lambda\eta_c)}{\lambda\eta_c} - \cos(\lambda\eta_c)\right) \tag{58}$$

from equations (33) and (35). Another condition is that $B_\theta(r = R_c) = 0$. This condition is written as

$$\tan(\lambda\eta) = \frac{\lambda\eta}{1-(\lambda\eta)^2}. \tag{59}$$

Equation (59) determines λ and then the parameter H_0 is obtained from equation (58). Note that the equation (59) has an infinite number of roots (see fig. 4 in Low 1984a). The first root for $\eta > 0$ arises at $\lambda\eta = \lambda\eta_1 \simeq 2.7$ and the second root does at $\lambda\eta = \lambda\eta_2 \simeq 6.1$. The first root corresponds to the position of the centre of the flux ropes. We take the second root as the contact surface, i.e. $\eta_c = \eta_2$ (z_1 in fig. 4 of Low 1984a) throughout this paper. The parameter H_0 is then determined from equation (58) as $H_0 \simeq 0.81$.

Another constraint on the parameter comes from pressure balance across the contact discontinuity. The pressure P_o consists of three component of the pressure, P_A, P_Q and P_i. P_A and P_Q are exactly zero at $r = R_c$ since $\tilde{A}|_{\eta=\eta_c} = \partial\tilde{A}/\partial\eta|_{\eta=\eta_c} = 0$. P_i should be smoothly connected with P_s at the contact surface. From this condition, the parameter P_0 is expressed as

$$P_0 = \frac{(1-\xi\eta_c^2)^2}{4\nu^3}\left(\frac{GM}{\eta_c} - \frac{\mu}{\sqrt{1-\xi\eta_c^2}}\right)^4. \tag{60}$$

Here we used equations (45) and (53).

The remaining parameters are $\xi, \eta_c, R_0, \alpha_n, n, \nu$ and μ, where ξ denotes the scaling of time and radius and η_c describes the velocity of the contact surface. Equation (51) determines R_0 by prescribing the shock radius when self-similar expansion starts. The twist injection at the central star determines the amplitude α_n and the Fourier mode number n of the toroidal magnetic fields. A constant ν which appears in equation (43) denotes the entropy of the isotropic plasma in the outflow region $r \leqq R_c$. The density at the contact surface when self-similar expansion starts determines the constant μ which appears in equation (46).

4 PHYSICAL PROPERTIES OF THE SELF-SIMILAR EXPLOSIONS

First, we concentrate on the structure of the magnetic loops in $r \leqq R_c$. Fig. 2 shows contours of the magnetic flux $\tilde{A}$ (left-hand panel) and the toroidal magnetic fields (right-hand panel) in the $\eta - \theta$ plane. The parameters are $\eta_c = \lambda$ and $\xi = 1$. The poloidal mode number of the toroidal magnetic fields is $n = 1$. We can see the flux rope structures emerging inside the expanding magnetic loops. The centre of the flux

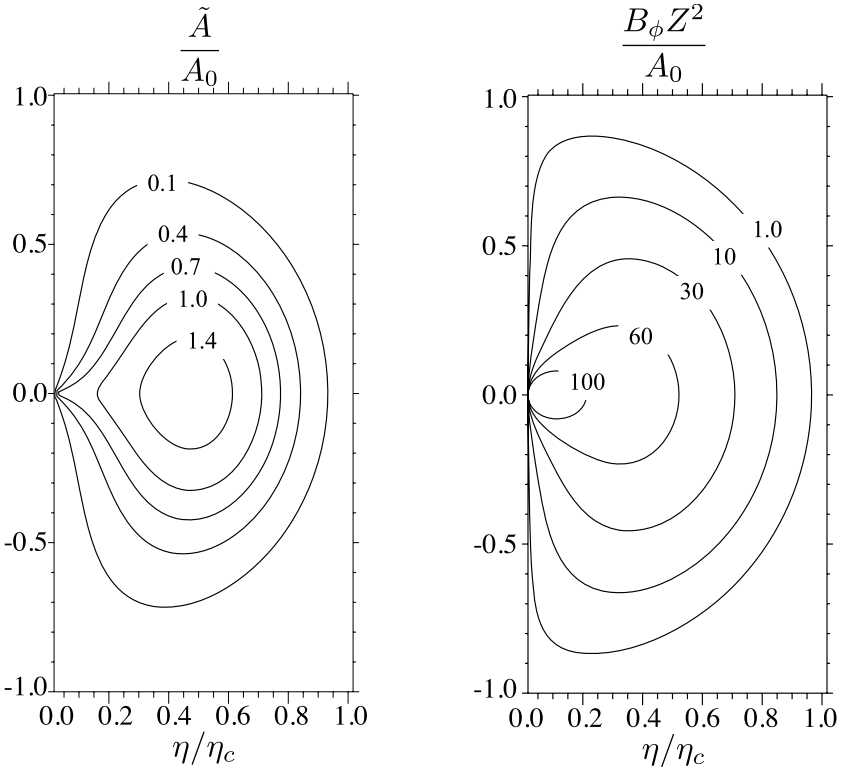

Figure 2. Contour plots of the magnetic flux $\tilde{A}$ (left-hand panel) and the toroidal magnetic fields. The contact surface is situated at $\eta/\eta_c = 1$. The parameters are taken as $\eta_c = \lambda, \xi = 1$ and $n = 1$.

ropes is situated at $\eta = \eta_1 (\eta_1 \simeq 0.44\ \eta_c)$. Since the magnetic fields have both poloidal and toroidal components, they describe the twisted flux ropes. The flux ropes rise in the $+ r$ direction with time. In the limit of $t \gg r$, the magnetic fields are represented as

$$\lim_{t\to\infty} \boldsymbol{B} = \frac{2A_0 H_0}{r^2} \cos\theta\ \boldsymbol{e}_{\rm r}, \tag{61}$$

from equations (33)–(35). The toroidal magnetic fluxes are diluted by the expansion according to the flux conservation equation. The configuration of the magnetic fields approaches that of the split monopole.

Fig. 3 shows contours of the gas pressure (left-hand panel) and the density (right-hand panel) in the $\eta - \theta$ plane. Contributions from the isotropic plasma, P_i and D_i, are subtracted, so that the pressure and the density can be negative in these panels. The set of the parameters is the same as those in Fig. 2. Accompanying the flux ropes, low-density voids are generated. The toroidal magnetic fields can create such voids. As mentioned at the end of Section 2, since the force balance is attained in our self-similar solutions, the Lorentz force by the poloidal magnetic fields should balance with the gas pressure gradient force and the toroidal magnetic pressure gradient force. This indicates that the gas pressure decreases as the toroidal magnetic pressure increases. Such voids exert the buoyancy force on the plasma in radial direction. Fig. 3 shows that the pressure gradient force ahead of the voids balances the buoyancy force.

Next, we consider the isotropic part of the outflowing plasma expressed in equations (45) and (46). When the constant μ is exactly zero, the plasma distribution reduces to that in hydrostatic states. The scaling comes from the assumption of adiabatic expansions with the polytropic index of $\Gamma = 4/3$. When μ is not zero, the plasma distribution differs from that in the hydrostatic states. When the flow speed is non-relativistic, i.e. $\sqrt{\xi}\eta \ll 1$, the solutions reduce to those in non-relativistic MHD obtained by Low (1984a). Since the enthalpy contributes to the plasma inertia, the correction term $(1 - \xi\ \eta^2)^{-1/2}$ arises in the relativistic MHD. The plasma tends to be hydrostatic since $\sqrt{\xi}\eta \ll 1$ when $t \gg r$.

In front of the outflow region, the ambient plasma is compressed by the shocks at $r = R_{\rm s}$ and is accumulated in the post-shock region ($R_{\rm c} \leqq r \leqq R_{\rm s}$). The contact surface at $R_{\rm c} = \sqrt{\xi}\eta_{\rm c} t$ divides the outflowing plasma from the shocked plasma. Since we assumed that the post-shock gas evolves self-similarly according to the same basic equations for the outflow region, the contact surface has the constant velocity $v_{\rm c} = \sqrt{\xi}\eta_{\rm c}$. The expansion speed of the shock radius $\mathrm{d}R_{\rm s}/\mathrm{d}t$ is, however, not constant but it increases with time. The time evolution of the shock radius is expressed by equation (51). Fig. 4 shows the radial profile of the outflow Lorentz factor. Dashed, dotted and dot–dashed curves denote the Lorentz factor at $t = 10$, 25 and 40, respectively. The thick curve denotes the time evolution of the shock Lorentz factor $\Gamma_{\rm s}$, while the thin solid curve the time profile of the outflow Lorentz factor at the shocks ($\gamma|_{r=R_{\rm s}}$). The value of the parameter R_0 is $R_0 = 1.78 \times 10^{-4}$, which corresponds to $\gamma(t = 5) = 8$. The shock Lorentz factor is larger than the outflow Lorentz factor at $r = R_{\rm s}$ by a factor of $\sqrt{2}$, as expected from relativistic strong gas dynamical shocks (see equation 50). The undisturbed plasma is abruptly heated up by the shocks. Plasma velocity suddenly becomes zero ahead of the shocks ($r > R_{\rm s}$) where the undisturbed plasma exists.

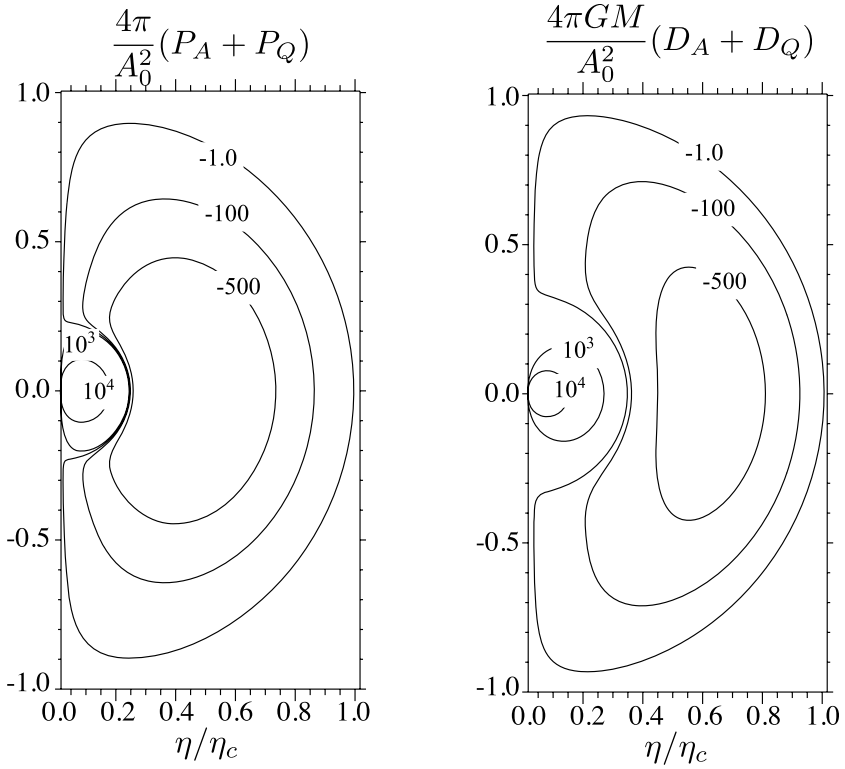

Figure 3. Contour plots of the pressure (left-hand panel) and the density (right-hand panel). The contribution from the isotropic plasma is subtracted. The contact surface is situated at $\eta/\eta_c = 1$. The parameters are taken as $\eta_c = \lambda, \xi = 1, n = 1$ and $\mu = 0$.

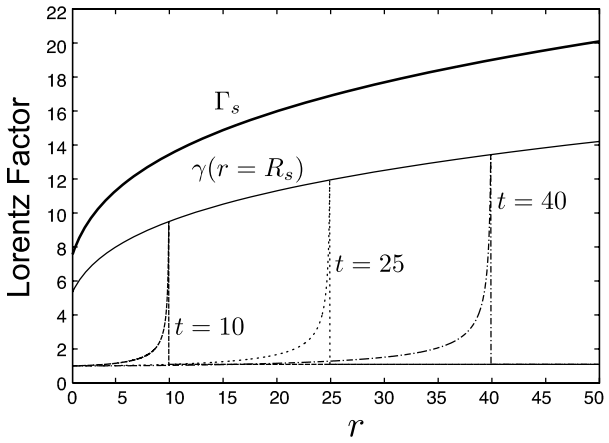

Figure 4. Radial profile of the outflow Lorentz factor. Dashed, dotted and dot–dashed curves show the outflow Lorentz factor at $t = 10$, 25 and 40, respectively. The thick solid curve shows the shock Lorentz factor, while the thin solid curve the maximum Lorentz factor of the outflow. The value of the parameter R_0 is taken to be $R_0 = 1.78 \times 10^{-4}$, which corresponds to $\gamma(t = 5) = 8$.

As the shock propagates in the undisturbed plasma, the shock surface is accelerated. The shock Lorentz factor and the shock radius can be expressed as

$$\Gamma_s \simeq \left[\frac{(1+\sqrt{2})^{\sqrt{2}}}{6}\right]^{1/4} \left(\frac{t}{R_0}\right)^{1/4} \simeq 0.87 \left(\frac{t}{R_0}\right)^{1/4}, \tag{62}$$

$$R_s \simeq t, \tag{63}$$

respectively. Here we approximate $v \simeq 1$ to obtain the first equality in equation (62). While the shock surface moves with almost constant speed $\simeq 1$, the shock Lorentz factor increases with time with the power-law index of 0.25. This result comes from the density profile of the undisturbed plasma. As shown later, the undisturbed plasma density decreases with radius as $r^{-3.5}$ (see equation 64). Shapiro (1979) showed that when $\rho \propto r^{-\delta}$, the flow is accelerated when $\delta > 3$. Although we take into account the gravity from the central star, which is not included

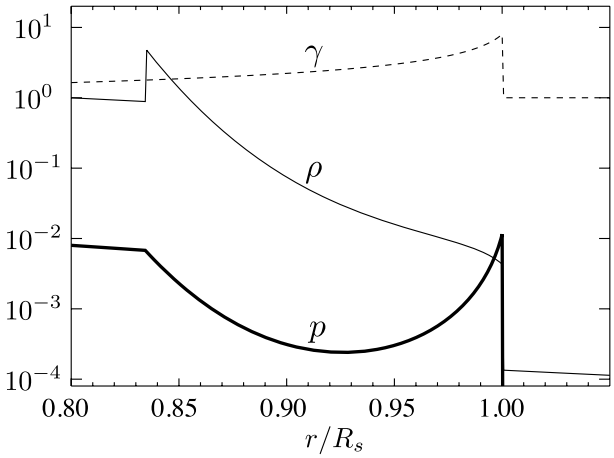

Figure 5. Radial profiles of the plasma pressure (thick solid curve), the plasma density (thin solid curve) and the Lorentz factor (dashed curve). Radius is normalized by the shock radius R_s. The contact discontinuity is situated at $R_c/R_s \simeq 0.834$. We take $\Gamma_s = 8\sqrt{2}$ and $\mu = 0$.

in Shapiro (1979), the gravitational force is smaller than the pressure gradient force in this region. Thus, their relation can be adopted in our analysis. The outflow is gradually accelerated when $\delta \simeq 3.5$.

Next, we consider the radial profile of the plasma pressure and the density. Fig. 5 shows the radial profile of the pressure p (thick solid curve), the density ρ (thin solid curve) and the outflow Lorentz factor (dashed curve) on the equatorial plane. The horizontal axis denotes the radius normalized by the shock radius R_s. The shock Lorentz factor is taken as $\Gamma_s = 8\sqrt{2}$. We take $\mu = 0$ for simplicity. The other parameters are $\xi = 1, R_0 = 1.3 \times 10^{-4}, \alpha_n = 0$ and $A_0 = 0$. The contact surface is situated at $R_c \simeq 0.834 R_s$. Behind the contact surface, the gas pressure and the density decrease with radius as $\propto r^{-4}$ and $\propto r^{-3}$, respectively.

The density jump appears at $r = R_c$, while the pressure is continuous (contact surface). The swept-up ambient plasma is accumulated in region $R_c \leqq r \leqq R_s$. The plasma density in the post-shock region ($0.834 < r/R_s < 1$) is larger than that in the outflow region. The strong pressure gradient force in this post-shock region pushes the plasma in $+r$ direction. The pressure gradient force balances with the inertia of the accumulated plasma. Thus, the plasma flows towards $+r$ direction with the inertial velocity.

Ahead of the contact discontinuity, a strong shock appears at $r = R_s$. We assumed the strong shock and neglected the ambient plasma pressure. The plasma is abruptly heated up by the shock. The ambient plasma density jump also appears at the shocks. The density of the shocked gas is larger than that of the ambient plasma by a factor of 32 for $\Gamma_s = 8\sqrt{2}$ as expected from the relativistic Rankin–Hugoniot relations (see equations 49 and 50). The density of the undisturbed plasma is described by equation (56). From this equation, the density can be approximately represented by the power law of r as

$$\rho(r) \simeq \frac{3P_0}{8\sqrt{R_0}\xi^2}\sqrt{\frac{(1+\sqrt{2})^{\sqrt{2}}}{6}K(1)r^{-\frac{7}{2}}}. \tag{64}$$

Here, we approximate $v_r(r = R_s) \simeq 1$ for relativistic flows. The density decreases with radius with the power-law index of -3.5. The ambient plasma density decreases slightly faster than that inside the shocks ($\propto r^{-3}$). The shock Lorentz factor thus increases with radius (Shapiro 1979).

Next, we consider the total energy contained within the spherical surface R_s. Let $\mathcal{E}$ be the total energy in $r < R_s$. As shown in Takahashi et al. (2009), the virial theorem can be applied for the relativistic inertial flow:

$$\mathcal{E} = \mathcal{K} - (3\Gamma - 4)U_{\rm th} + \int \frac{\partial \boldsymbol{S}\cdot\boldsymbol{r}}{\partial t}{\rm d}V + \int p\boldsymbol{r}\cdot{\rm d}\boldsymbol{\mathcal{A}} - \frac{1}{8\pi}\int \left\{2\left[(\boldsymbol{r}\cdot\boldsymbol{E})(\boldsymbol{E}\cdot d\boldsymbol{\mathcal{A}}) + (\boldsymbol{r}\cdot\boldsymbol{B})(\boldsymbol{B}\cdot d\boldsymbol{\mathcal{A}})\right] - (\boldsymbol{E}^2+\boldsymbol{B}^2)(\boldsymbol{r}\cdot d\boldsymbol{\mathcal{A}})\right\}, \tag{65}$$

where

$$\mathcal{K} = \int {\rm d}V \rho\gamma^2, \tag{66}$$

$$U_{\rm th} = \int {\rm d}V \frac{p}{\Gamma - 1} \tag{67}$$

and $\boldsymbol{S}$ shows the Poynting flux. Here $\boldsymbol{\mathcal{A}}$ denotes expanding spherical surface at $r = R_s(t)$. The third, fourth and fifth terms of the right-hand side of equation (65) represent the Poynting flux, the work done by the gas pressure and the work done by the Maxwell stress, respectively.

Let us evaluate the non-kinetic part of the energy, $\mathcal{E}' = \mathcal{E} - \mathcal{K}$. The second term in the right-hand side of equation (65) is zero because the polytropic gas index is $\Gamma = 4/3$. The fifth term of (65) is zero since the electromagnetic fields vanish at $r = R_s$. The third term also becomes zero after the straightforward calculations. Thus, the non-kinetic part of the energy can be evaluated as

$$\mathcal{E}'(t) = \left.\frac{8\pi}{3}\rho_0\Gamma_s^2 R_s^3\right|_{r=R_s} = \left.\frac{4\pi}{3}\rho\gamma R_s^3\right|_{r=R_s}. \tag{68}$$

Here, we used equations (48) and (50). The energy $\mathcal{E}'$ does not depend on the amplitudes of the magnetic fields. As shown in Section 3, the plasma density (pressure) consists of three parts, D_A, D_Q and D_i(P_A, P_Q and P_i). While the components D_A and D_Q depend on the magnetic field strength, D_i is independent of them. D_A and D_Q do not contribute to the non-kinetic part of the energy from equation (65) since they are exactly zero at $r = R_c$. This indicates that the plasma interacting with the magnetic fields is in marginally stable state. Low (1982a) showed that the inertial flow with the polytropic index $\Gamma = 4/3$ represents the marginally stable state in non-relativistic MHD. This situation is also valid for the relativistic MHD. Total energy contained inside the shocks is thus independent of the strength of the magnetic fields.

By substituting equations (62) and (64) into equation (68), the time evolution of the energy $\mathcal{E}'$ is written as

$$\mathcal{E}' = \frac{(1+\sqrt{2})\pi}{6}\frac{K(1)}{\xi}\frac{P_0}{R_0}, \tag{69}$$

where we used equations (62), (63) and (64). Note that the non-kinetic part of the energy $\mathcal{E}'$ is positive. This means that plasma speed exceeds the escape velocity determined by the gravitational potential.

The kinetic energy $\mathcal{K}$ given in equation (66) is expressed as

$$\mathcal{K} = 2\pi \int \mathrm{d}\theta \sin\theta \int \mathrm{d}\eta \, \frac{D(\eta,\theta)}{\sqrt{1-\eta^2}}, \tag{70}$$

where we used equations (16) and (23). Note that equation (70) depends on time through η. When we integrate inside the sphere with radius $r = R_s$, the integration is carried out in [0, η_s] in the self-similar space. Since the flow is relativistic, i.e. $v_r \simeq 1$, $\eta_s \simeq 1/\sqrt{\xi}$ is constant with time. Thus, both non-kinetic and kinetic energies are constant with time. Strictly speaking, the total energy should increase with time since the shock surface sweeps up the ambient plasma. The rest mass energy of the swept-up plasma contributes to the increase in the total energy. This energy is, however, negligible because we assume the strong shocks. From equation (48), the rest mass energy density of the undisturbed ambient plasma is smaller than the kinetic energy density of the shocked gas by a factor of Γ_s^4 and negligibly small. [Note that the relations 48–50 are correct with the accuracy of $\mathcal{O}(1/\Gamma_s^2)$]. For the same reason, $\mathcal{E}'$ is also independent of time with the accuracy of $\mathcal{O}(1/\Gamma^2)$. Using these facts, the shock Lorentz factor is expressed as

$$\Gamma_s = \sqrt{\frac{3}{8\pi}}\mathcal{E}'^{\frac{1}{2}}\rho_0^{-\frac{1}{2}}(r = R_s)R_s^{-\frac{3}{2}} \tag{71}$$

from equation (68). This result is equivalent with equation (16) in Shapiro (1979). Although our solutions include the magnetic fields and the gravity from the central star, they do not contribute to the total energy because the system is in a marginally stable state. Thus, only the hydrodynamical (isotropic) part contributes to the total energy. By inserting equations (63) and (64) into this equation, we obtain $\Gamma_s \propto r^{1/4}$ again (see equation 62). The shock is thus accelerated when it propagates in the ambient plasma.

5 NUMERICAL SIMULATIONS

In this section, we show results of relativistic MHD simulations to study the stability of our solutions. For this purpose, we use the analytical solutions as the initial conditions of the numerical calculations. The relativistic MHD equations are solved in two dimensions using polar coordinates (r, θ). We assume axisymmetry $(\partial/(\partial\phi) = 0)$. The number of grid points is $(N_r, N_\theta) = (3600, 360)$ on the domain of $R_{in} \equiv 1 \leqq r \leqq 50$ in normalized unit and $0 \leqq \theta \leqq \pi$. The grid sizes are $\Delta r = 1.39 \times 10^{-2}$ and $\Delta\theta = 8.72 \times 10^{-3}$. We use the HLL (Harten, Lax & van Leer 1983) method to calculate numerical fluxes. We utilize the modified Corner Transport Upwind (CTU) method (Mignone & Bodo 2006) to achieve the second-order accuracy in space. In our analytical solutions, the strong shock is expected. Such a strong shock can induce the numerical oscillations. To avoid the problem, we utilize the harmonic mean for smoother prescription (van Leer 1977). We use the constraint-transport method to satisfy the no-monopole condition. We impose the outflow boundary conditions in outer radial boundary at $r =$ 50 and the symmetric condition at the axes at $\theta = 0, \pi$. The inner boundary conditions are imposed at $r = R_{in}$ by applying the time-dependent analytical solutions. We solve the whole region covering $\theta \in [0, \pi]$, although our analytical solution is symmetric at $\theta = \pi/2$. So we can check whether our code maintains this symmetry. The parameters are the initial time $t_0 = 11.0, R_s(t = t_0) = 10.8$, $R_c(t = t_0) = 8.83$, $r_g \equiv GM = 0.148$, $\xi = 1, R_0 = 2.58 \times 10^{-3}, \alpha_1 = 0.1, n = 1, \mu = 0$ and $\rho_i R_i^4/A_0^2 = 100$. The initial maximum Lorentz factor [$\gamma_s(t = t_0, r = R_s(t = t_0))$] is 5. Radius and time are normalized by the inner radius R_{in} and its light crossing time, respectively.

To obtain the analytical solutions, the ambient plasma pressure p_0 is not specified because we adopted Ranking–Hugoniot relations for a strong shock, so that the ambient pressure is negligible. However, in order for the ambient plasma to be in hydrostatic equilibrium, the gas pressure gradient force should balance with the gravitational force of the central star. Since it is a hard task to reconstruct the self-similar solutions taking into account the ambient plasma pressure, we use the analytical solutions obtained by using approximate Rankin–Hugoniot relations given in equations (48)–(50) as the initial conditions and the ambient pressure are taken initially to be constant, which means that the ambient plasma is not in hydrostatic equilibrium. The ambient plasma slowly falls towards the central star due to the gravity of the central star. The parameters we used in numerical simulations are taken so that the free-fall time t_{ff} is much larger than the dynamical time t_d (typically $t_{ff}/t_d \simeq 10^3$). Thus, the free-fall motion of the ambient plasma does not affect the dynamics of the expanding magnetic loops. Stone & Norman (1992) adopted a different method for this problem such that the gravitational force is artificially subtracted in the ambient plasma to numerically recover the solutions of the non-relativistic coronal mass ejection obtained by Low (1984a). We confirmed that the results obtained by the method proposed by them are consistent qualitatively and quantitatively with those including the gravity in the ambient

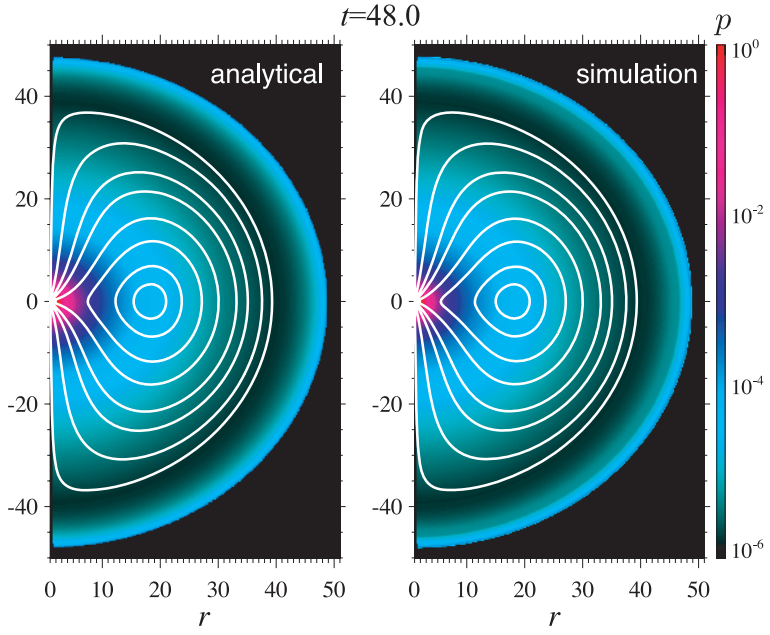

Figure 6. Colour contour shows the gas pressure profile and curves show the magnetic field lines for analytical solutions (left-hand panel) and numerical results (right-hand panel).

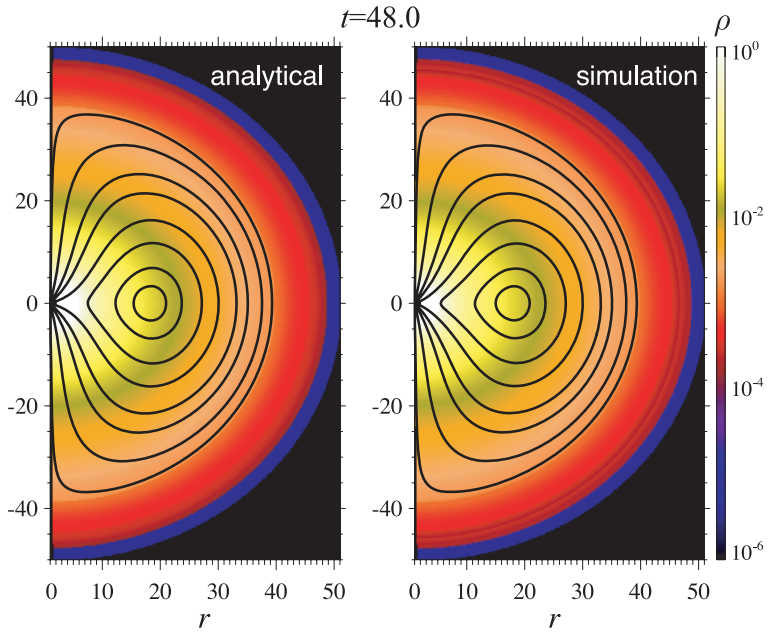

Figure 7. Colour contour shows the density profile and curves show the magnetic field lines for analytical solutions (left-hand panel) and numerical results (right-hand panel).

plasma. The ambient plasma pressure, which is not specified in the analytical solutions, is taken to be so small ($p_0 = 10^{-8}$) that it does not affect the dynamics of the outflows.

Fig. 6 shows the pressure profile (colour) and the magnetic field lines (curves) at $t = 48$. The left-hand panel shows analytical solutions and the right one numerical results. Fig. 7 shows the density profile (colour). The magnetic field lines in Figs 6 and 7 are depicted as the isocontours of the flux function. The levels of the isocontours are identical in both figures.

As time goes on, the magnetic loops containing the flux ropes expand in radial direction. The flux ropes carry the toroidal magnetic fields. The ambient matter inflowing through the shock is compressed and accumulated between the contact discontinuity and the shock. The numerical results excellently recover the analytical solutions.

Fig. 8 shows the shock structure on the equatorial plane at $t = 48$. Left-hand panel shows the Lorentz factor and the right one the density and the pressure. Thin solid curves denote the analytical solutions, while thick solid curves the numerical results. At this time, the maximum Lorentz factor is $\gamma = 7.2$ for the analytical solution. The peak Lorentz factor in the numerical simulation is, however, $\gamma = 6.2$. The difference

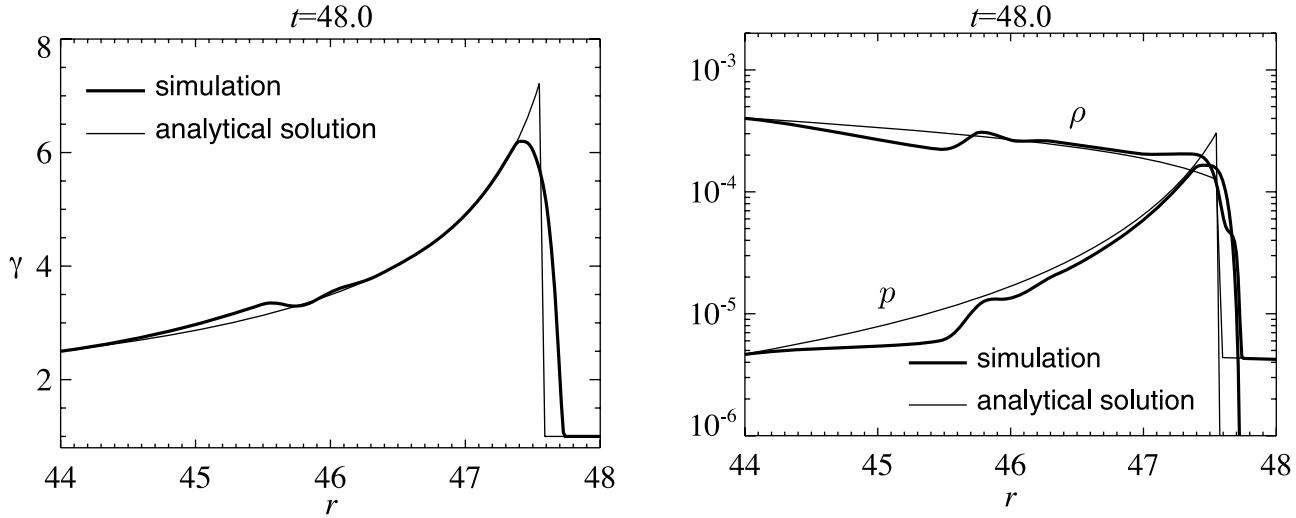

Figure 8. The Lorentz factor (left-hand panel) and the density and pressure profiles (right-hand panel) on the equatorial plane at $t = 48$. Thick curves denote the numerical results, while thin curves denote analytical solutions.

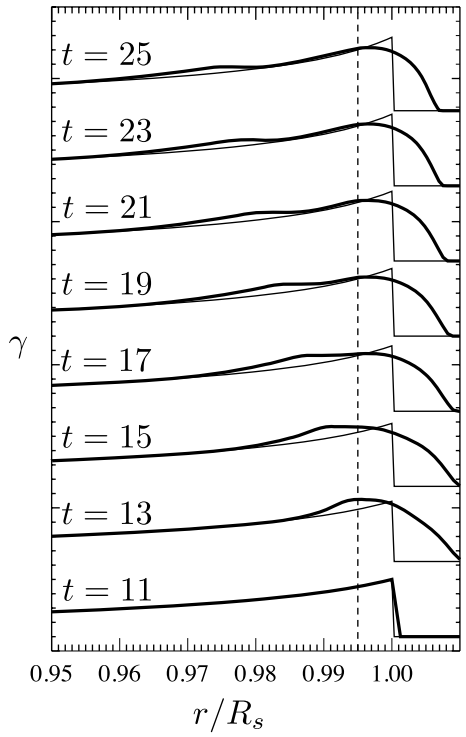

Figure 9. Time evolution of the Lorentz factor on the equatorial plane. Thick curves show the numerical results, and the thin curves show the analytical solutions. Dashed curve shows the reference radius $r = r_* = 0.995R_s$.

comes from the shock flattening in the simulations. Note that we adopt the harmonic mean to evaluate primitive variables on the cell surface. This method is more diffusive than other interpolation methods, such as the Monotone Upstream-centered Scheme for Conservation Laws (MUSCL)-type interpolations. Although we utilize this method to avoid numerical oscillations at the strong shocks, it decreases the peak Lorentz factor. Also the density and the pressure profiles are diffused (right-hand panel of Fig. 8). Another reason comes from the assumption of strong shocks adopted to derive the approximate Rankin–Hugoniot relations (48)–(50). These relations are correct with an accuracy of $\mathcal{O}(1/\gamma^2)$. Since we take the initial Lorentz factor at the shock as $\gamma = 5$, a few per cent error arises from the approximations.

Such a numerical diffusion produces the sound waves from the shocks. Fig. 9 shows the radial profile of the Lorentz factor on the equatorial plane from the initial state at $t = t_0 = 11$ to $t = 25$ with the interval $\delta t = 2$. Thick and thin solid curves show numerical results and analytical solutions, respectively, while the dashed line denotes a reference radius $r_* = 0.995R_s$ (see Fig. 10). After the simulation goes on, the shock is flattened due to the numerical diffusion, generating the sound waves propagating inwards and outwards from the shock. The compressional waves extract a part of the fluid kinetic energy from the shock, resulting in the increase in the numerical velocity behind/ahead

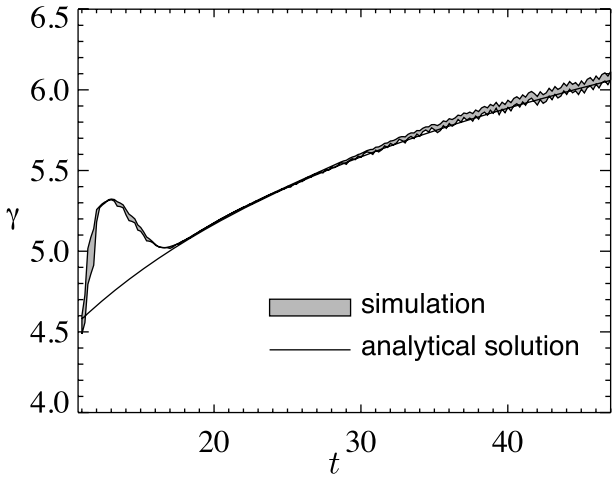

Figure 10. Time evolution of the Lorentz factor at $r \equiv r_* = 0.995R_s$. Horizontal axis shows the time and vertical axis shows the Lorentz factor on the equatorial plane. Solid curve shows the analytical solutions. Grey contours show the Lorentz factors at the grid points closest to the reference radius $r_* = 0.995R_s$.

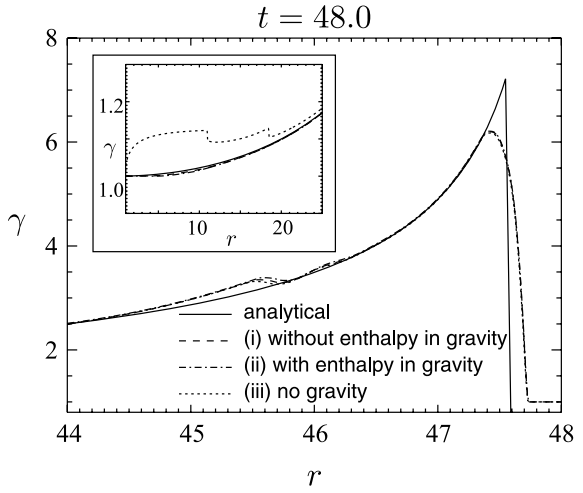

Figure 11. The dependence of the equatorial Lorentz factor at $t = 48$ on models of the gravity, (i) $-GM\rho\gamma^2/r^2$ (dashed), (ii) $-GM\rho h\gamma^2/r^2$ (dash–dotted) and (iii) without gravity. Solid curve denotes the analytical self-similar solutions. The inset shows solutions in the different range $1 \leq r \leq 25$.

of the shock from the analytical solutions. As the wave propagates away from the shock front, the radial profiles approach those of analytical solutions. Note that the amplitudes of the inwards propagating wave decreases with time because the wave conserves the wave energy density $E_w = \rho\gamma^2$. Since the density increases inwards, the velocity deviation $\delta\gamma$ decreases as the wave propagates.

Fig. 10 shows the time evolution of the Lorentz factor. Solid curve shows the analytical solution. We measure the Lorentz factor at a reference radius $r_* = 0.995R_s(t)$ to avoid the effects of the shock flattening. Since the simulation is carried out at discrete grid points, we plot the range of the Lorentz factors of the mesh points closest to the reference radius $r_* = 0.995R_s$ (grey contours). The numerical results deviate from the analytical solution when $t < 13$ because the flattening of the shock front and the emission of the sound waves temporarily increase the velocity behind the shock. The numerical results are, however, consistent with the analytical solutions after the sound waves propagate away ($t \gtrsim 18$). Then, the Lorentz factor increases with time as $\gamma \propto t^{1/4}$.

Next, we numerically verify the approximation of neglecting the thermal enthalpy term h_N in the gravitational force $-GM\rho h\gamma^2/r^2 = -GM\rho\ (1 + h_N)\gamma^2/r^2$ (Mobarry & Lovelace 1986; Meliani et al. 2006). When we derive analytical solutions of the self-similar expansion, we neglect h_N in the gravity. Although the specific thermal enthalpy h_N becomes larger than unity behind the strong shock ($p_s/\rho_s \simeq \Gamma_s \gg 1$, see equations 48–50), the gravitational force itself becomes small compared to the other forces in the self-similar stage when $R_s \gg r_g$. To evaluate the contribution of the gravity, we carried out numerical simulations for three models of the gravity, i.e. (i) $-GM\rho\gamma^2/r^2$, (ii) $-GM\rho h\gamma^2/r^2$ and (iii) without gravity.

Fig. 11 shows the radial profiles of the Lorentz factor on the equatorial plane at $t = 48$ with different models of the gravity. Solid curve shows the self-similar solutions, while dashed, dash–dotted and dotted curves show the numerical results for models (i)–(iii), respectively. An inset shows solutions in the different range of r, $1 \leqq r \leqq 25$. Behind the shock, numerical results are almost independent of the models of the gravitational force, indicating that the gravitational force is much smaller than the other forces. As we mentioned in Section 2, the ratio of the gravity for the thermal enthalpy to the plasma inertia decreases with radius (see equation 25). The ratio r_g/R_s is 0.01 at the initial state

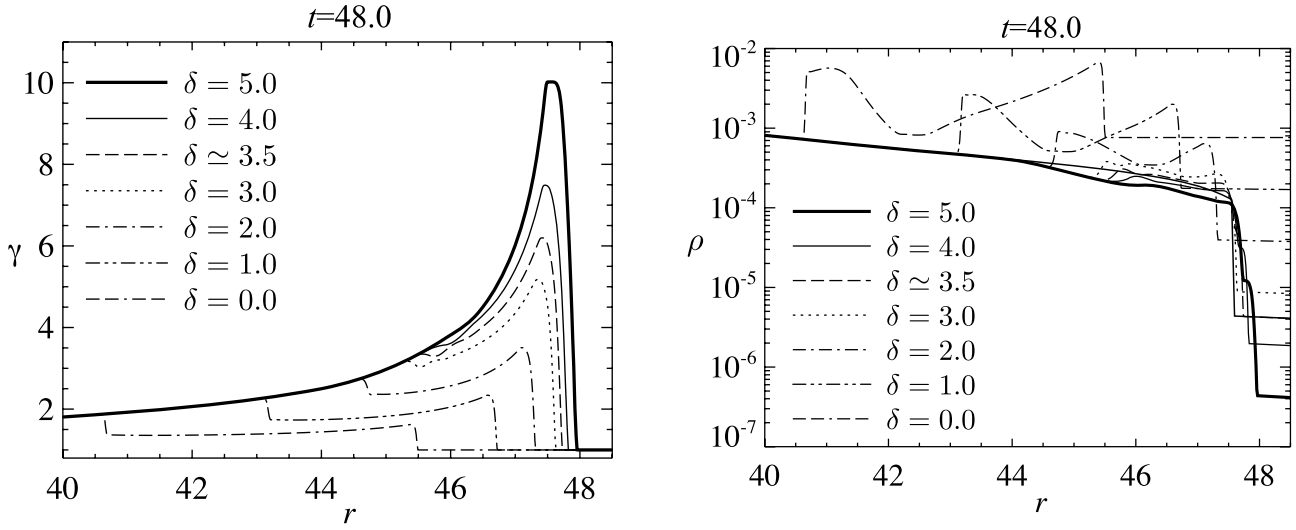

Figure 12. The dependence of the equatorial Lorentz factor (left-hand panel) and the density profile (right-hand panel) at $t = 48$ on the density parameter of the ambient gas δ. Dashed curves denote the numerical results for initial condition given by the analytical solutions ($\delta \simeq 3.5$). The other curves depict those for $\delta = 5, 4, 3, 2, 1, 0$.

$t = t_0$ and 3×10^{-3} at the final state $t = 48$ in our simulations. Thus, the gravity for the thermal enthalpy is negligible. This explains why the numerical results are independent of the gravity models. The specific thermal enthalpy h_N is larger than unity just behind the shock, but the gravitational force is much smaller than the other forces when $r_g \ll R_s$.

Although the gravity becomes important in the region where $r_g < r \ll R_s$, the thermal enthalpy is negligible in this region (i.e. $h_N \ll 1$). Thus, we can neglect the contribution of h_N in the gravity (see the inset of Fig. 11). We note that the numerical results for model (iii) deviate from the analytical solutions in this region. The plasma is accelerated in radial direction by the pressure gradient force, leading to the formation of shocks ($r \simeq 18.5$). Since we use analytical solutions for inner boundary conditions at $r = R_{in} = 1$, the plasma is supplied from the inner boundary. When the plasma is not confined by gravity, the outflowing plasma forms second shocks at $r \simeq 11$.

When R_s is close to r_g, the contribution of h_N in the gravity is not negligible, but we have to take into account the general relativistic effects in such region, so that the characteristic length r_g enters into the formulations. In such regime, no self-similar solutions can be obtained. It is out of the scope of this paper to obtain solutions in this regime.

Next, we carried out simulations with different density profiles of the ambient plasma to study the generality of the analytical solutions and the effects of the ambient density distribution on the loop dynamics. We substitute the density profile given in equation (56) with the power-law profile as

$$\rho(r) = \rho_0(r = R_{s,0}) \left(\frac{r}{R_{s,0}} \right)^{-\delta}, \tag{72}$$

where $R_{s,0} = R_s(t = t_0)$. The analytical solutions correspond to $\delta \simeq 3.5$. We study several cases ($\delta = 0, 1, 2, 3, 4, 5$). The initial condition is given by the analytical solutions inside the shock.

The dependence of the equatorial Lorentz factor (left-hand panel) and the density profile (right-hand panel) at $t = 48$ on the density parameter of the ambient gas δ is plotted in Fig. 12. Dashed curve denotes the numerical results for initial conditions given by the analytical solutions ($\delta \simeq 3.5$). Other curves depict those for $\delta = 5, 4, 3, 2, 1, 0$. The peak Lorentz factor decreases as δ decreases. This is because the shell becomes massive for a smaller δ by sweeping up the larger ambient plasma. The swept up plasma is accumulated behind the shock surface. The inertia from the excess plasma accumulated behind the shock decelerates the outflows and creates another discontinuity behind the shock. The discontinuity can be considered as the reverse shock. The compression ratio of the reverse shock is larger for the denser ambient plasma.

Time evolution of the equatorial Lorentz factor at the reference radius r_* is shown in Fig. 13. Circles depict the numerical results for the initial conditions given by the analytical solutions for $\delta \simeq 3.5$. Other symbols show the numerical results for $\delta = 5, 4, 3, 2, 1, 0$. The Lorentz factor is evaluated at $r_* = 0.995 r(\gamma_{max})$, where $r(\gamma_{max})$ is the radius where the Lorentz factor is its maximum.

The peak Lorentz factor increases with time when $t < 13$. This increase comes from the emission of the sound waves propagating from the shock front. When $t > 18$, the peak Lorentz factor increases with time when $\delta > 3$. The critical value of δ whether the outflow is accelerated or not can be evaluated from the mass conservation. The plasma density of the outflow decreases with radius by r^{-3} according to the mass conservations (see equation 16). The rest mass energy of the ambient plasma accumulated in the shell thus increases with time when $\delta < 3$. On the other hand, when $\delta > 3$, the outflow is accelerated since the plasma inertia of the outflow decreases with time. Naively, we can understand these processes from equation (71). According to this equation, the flow is accelerated when the ambient plasma density decreases faster than r^{-3}. When $\delta = 5$, the shock is accelerated and its Lorentz factor is proportional to the radius ($\simeq$ time). It indicates that the flow expands freely. The influence of the ambient plasma is almost negligible. Piran, Shemi & Narayan (1993) derived the self-similar solution of

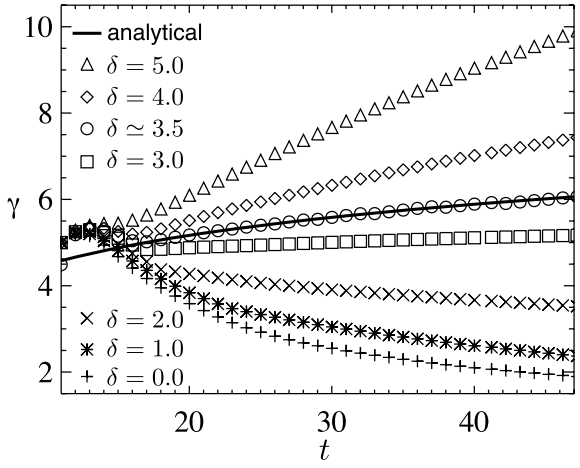

Figure 13. Time evolution of the Lorentz factor at the reference radius r_*. Circles depict the numerical results for the initial conditions given by the analytical solution for $\delta \simeq 3.5$. Other symbols show the numerical results for $\delta = 5, 4, 3, 2, 1, 0$. The Lorentz factor is evaluated at $r_* = 0.995 r(\gamma_{\max})$, where $r(\gamma_{\max})$ is the radius where the Lorentz factor is its maximum.

the free expansion. The shock Lorentz factor then increases with radius linearly. The shock profile for $\delta = 5$ or a larger δ is consistent with the solution obtained by Piran et al. (1993). Inside the shock surface, our solutions are, however, not identical with their analytical solutions since our solutions include the magnetic fields and are intrinsically non-spherical.

6 SUMMARY AND DISCUSSIONS

We derived axisymmetric relativistic self-similar solutions of the magnetic flux rope expansion by assuming the purely radial flow and ignoring the stellar rotation. By taking the self-similar variable as $\eta = r/Z(t)$, the arbitrary function $Z(t)$ has a unique form given in equation (22). The MHD equations are then solved analytically.

The solutions obtained in this paper are the extension of our previous work (Takahashi et al. 2009) by considering the two discontinuities, the contact discontinuity and the shock. The contact discontinuity separates the outflowing plasma and the ambient plasma. The outgoing waves propagating in the ambient plasma form shocks.

Such self-similar solutions including two discontinuities are derived by Low (1984a) in non-relativistic MHD. Our solutions are the extension of their solutions to the relativistic MHD. For the non-relativistic case, the compression ratio at the shock is determined by the specific heat ratio. The specific heat ratio is taken as $\Gamma = 4/3$ in non-relativistic MHD equations. The system is marginally stable for the inertial flow. The compression ratio is then up to 7 for the strong shocks. In relativistic plasma, the sound speed is limited to $\sim$0.58 for the ideal gas. The differences between the upstream flow velocity and the downstream wave velocity are larger for the larger flow velocity. This fact results in forming the strong shocks, and the compression ratio can be larger than 7. The ambient plasma is abruptly heated by the strong shocks. The hot plasma is accumulated in the shell between the shocks and the contact discontinuity. Inside the contact discontinuity, the magnetic loops anchored to the central star are assumed to follow the flux rope solutions obtained by Low (1984a). The flux ropes are contained inside the global magnetic loops. Such magnetic field configuration can be expected for the SGR flares after the magnetic energy is dissipated (Lyutikov 2006).

We also carried out numerical simulations of two-dimensional relativistic MHD by using the self-similar solutions as the initial and inner boundary conditions. Since analytical solutions are obtained in this paper, we can apply them to check the accuracy of multi-dimensional relativistic MHD codes. Many previous authors reported that the relativistic MHD code is verified by using the one-dimensional shock tube problems. There are only a few standard multi-dimensional problems, such as the blast wave problem or the rotor problem. However, no exact solutions are known for these problems. We have shown that the self-similar solutions can be applied to check the accuracy of the relativistic MHD codes.

Numerical calculations show that the shock velocity strongly depends on the ambient plasma density. When the density profile is steeper than $\propto r^{-3}$, the shock Lorentz factor increases with radius. On the other hand, it decreases for profiles shallower than r^{-3}. Such a behaviour is expected from the consideration of the mass conservation (Shapiro 1979). The density inside the shocks approximately decreases with radius as $\propto r^{-3}$. When the decrease in the ambient plasma density is steeper than the shocked plasma density, the outflows can be accelerated. We can understand this from the energy conservation given in equation (71). The time dependence of the shock Lorentz factor is related to the ambient plasma density. When $R_s \simeq t$ and the ambient plasma density is represented by the power law on r ($\rho \propto r^{-\delta}$), the shock Lorentz factor is expressed as $\Gamma_s \propto r^{(3-\delta)/2}$. Numerical results agree with this relation. Especially when $\delta \geqq 5$, the shock Lorentz factor linearly increases with radius.

Finally, let us apply our results to the magnetar flares (Woods & Thompson 2006; Mereghetti 2008). In the following discussion, we concentrate on the extraordinarily energetic outbursts (giant flares) observed in SGRs. Although AXPs as well as SGRs would be magnetars,

the giant flares have not been detected from the AXPs. The reason would be that the giant flares are very rare events (1 per a few decades in the whole sky).

The shock Lorentz factor Γ_s is estimated from the mass ejected by the flare $M_{eje} \sim 4\pi\rho_0 R_s^3/3$, and equation (68) as

$$\Gamma_s \simeq 24 \left(\frac{\mathcal{E}'}{10^{46}\mathrm{erg}}\right)^{\frac{1}{2}} \left(\frac{M_{eje}}{10^{22}\mathrm{g}}\right)^{-\frac{1}{2}}. \tag{73}$$

The expansion speed of the magnetic loop is relativistic when $M_{eje} < 10^{22}$ g (see also Lyutikov 2006). The mass density behind the forward shock is estimated from equations (49), (50) and (73) as

$$\rho_s = 1.6 \times 10^{-4}\ \mathrm{g\ cm^{-3}} \left(\frac{\mathcal{E}'}{10^{46}\ \mathrm{erg}}\right)^{\frac{1}{2}} \left(\frac{M_{eje}}{10^{22}\ \mathrm{g}}\right)^{\frac{1}{2}} \left(\frac{R_s}{10^9\ \mathrm{cm}}\right)^{-3}. \tag{74}$$

The mass density in the ambient plasma $\rho_0 = \rho_s/(2^{3/2}\Gamma_s)$ estimated from equations (49), (50), (73) and (74) is much larger than the Goldreich–Julian density. Such dense coronal pair plasmas would be created by the pair production when the magnetically trapped fireball is formed on the surface of the magnetar (Beloborodov & Thompson 2007).

The temperature of the shocked gas is evaluated by using equation (48) as

$$T_s \simeq 2.8\ \mathrm{MeV} \left(\frac{\mathcal{E}'}{10^{46}\ \mathrm{erg}}\right)^{\frac{1}{2}} \left(\frac{M}{10^{22}\ \mathrm{g}}\right)^{-\frac{1}{2}}. \tag{75}$$

Here, we assume the pair plasma. Although the radiation spectrum of the initial spike in the giant flare is not well determined because of its short duration, the typical temperature indicated by the spectrum is a few 100 keV (Hurley et al. 2005), which is lower than T_s estimated from our analytical solutions. We have to note that the temperature at the photosphere T_{ps} should be smaller than T_s because the temperature decreases with decreasing the radius behind the shock (see Figs 5 and 8). The radius of the photosphere R_{ps} can be determined by the condition that the optical depth of the expanding magnetic loops τ_{ps} satisfies

$$\tau_{ps} = \int_{R_{ps}}^{R_s} \rho\tilde{\kappa}\gamma(1 - v\cos\theta)\,\mathrm{d}r = 1, \tag{76}$$

where θ is the angle between the velocity vector and the direction of the photon propagation (Abramowicz, Novikov & Paczynski 1991), and $\tilde{\kappa} = \sqrt{\kappa_{ff}(\kappa_{es} + \kappa_{ff})}$ is the effective opacity. Here, κ_{es} and κ_{ff} are the opacity for the electron scattering and the free–free absorption, respectively. We assume that the ambient plasma ($r > R_s$) is optically thin. The electron scattering is the dominant source of the opacity inside the shocks. This is because the plasma temperature is increased by the shock heating, so that the free–free opacity ($\rho T^{-3.5}$) is much smaller than that of the electron scattering.

We numerically integrate equation (76) assuming that $\theta = 0$, the expansion energy $\mathcal{E}' = 10^{46}$ erg and the mass of the central star $M = 1\,\mathrm{M}_\odot$, where $\mathrm{M}_\odot$ is the solar mass. The temperature at the photosphere T_{ps} calculated at $R = R_{ps}$ from the analytical solutions (equations 13, 15, 16, 53 and 54) can roughly be fitted by

$$T_{ps} \simeq 10 \left(\frac{\Gamma_s}{10}\right)^{-1.4} \left(\frac{R_s}{10^9\ \mathrm{cm}}\right)^{-1.3}\ \mathrm{keV}, \tag{77}$$

when $10 \lesssim \Gamma_s \lesssim 100$ and $10^7\ \mathrm{cm} \lesssim R_s \lesssim 10^{10}$ cm. The result is almost independent of the radius of the contact discontinuity (i.e. R_c/R_s). The temperature in the observer's frame is $T_{obs} = \gamma T_{ps} \simeq \Gamma_s T_{ps} \simeq 100$ keV when $\Gamma_s \simeq 10$. Here we assume $\gamma \simeq \Gamma_s$ since the photosphere is very close to the shock surface. This result is consistent with the observational results when $\Gamma_s \simeq 10$ and $R_s \simeq 10^9$ cm.

Such hot, relativistically expanding magnetic loops are expected to be formed with the help of the magnetic reconnections. According to the scenario by Lyutikov (2006), the magnetic reconnections inside the magnetic loops are responsible for the initial spike of the flares (see also Gill & Heyl 2010). Subsequently, the plasma is heated up by the shocks produced by the magnetic reconnection. By applying our models to the giant flares, the time evolution of the luminosity from expanding plasma is expressed as $L \propto T_{obs}^4 R_{ps}^2 \propto \Gamma_s^{-1.6} R_s^{-3.2}$ from $T_{obs} \sim \Gamma_s T_{ps}$ and equation (77). Here, we assumed $R_{ps} \simeq R_s$. Since $\Gamma_s \propto R_s^{(\delta-3)/2}$ from equations (71) and (72), we obtain $L \propto t^{-0.8(1+\delta)}$ because $R_s \propto t$ from equation (63). Terasawa et al. (2005) reported that the observed photon counts decreased exponentially with time after the initial spike. However, the photon counts at the earlier stage, whose decay time is very short ($\lesssim 100$ ms), is not inconsistent with the power-law decay.

In addition to the initial spikes, a hump is observed a few hundred seconds after the initial spike (Terasawa et al. 2005). It is considered that the energy is re-injected from the central star. We now consider another possibility for this hump. Before the magnetic energy release, the toroidal magnetic energy can be comparable to that of the poloidal magnetic fields inside the magnetic loops. When the magnetic reconnection takes place inside the magnetic loops, the magnetic energy of the poloidal magnetic fields is converted to the plasma energies, generating the twisted flux ropes. The toroidal magnetic field energy of the flux ropes does not dissipate in this process. When the twisted flux ropes cross the Alfvén radius ($\simeq$ light cylinder), the rest magnetic energy will be dissipated by interaction with the ambient global magnetic fields. The time-scale that a flux rope crosses the light cylinder and releases the magnetic energy is about $\sim$1 s, which is consistent with the observations. The energy dissipation at the light cylinder can be responsible for the humps. We need further study to verify these processes.

ACKNOWLEDGMENTS

We are grateful to an anonymous referee for improving our manuscript. We thank Hiroaki Isobe, Jin Matsumoto, Kazunari Shibata and Youhei Masada for useful discussions. Numerical computations were carried out on Cray XT4 at Center for Computational Astrophysics (CfCA) of

National Astronomical Observatory of Japan and on Fujitsu FX-1 at JAXA Supercomputer System (JSS) of Japan Aerospace Exploration Agency (JAXA). This work was supported by the Grants-in-Aid for Scientific Research of Ministry of Education, Culture, Sports, Science, and Technology (RM:20340040).

REFERENCES

Abramowicz M. A., Novikov I. D., Paczynski B., 1991, ApJ, 369, 175
Asano E., 2007, PhD thesis, Chiba Univ.
Beloborodov A. M., Thompson C., 2007, ApJ, 657, 967
Blandford R. D., McKee C. F., 1976, Phys. Fluids, 19, 1130
Burrows A., 1987, ApJ, 318, L57
Duncan R. C., Thompson C., 1992, ApJ, 392, L9
Gill R., Heyl J. S., 2010, MNRAS, 407, 1926
Gourgouliatos K. N., Lynden-Bell D., 2008, MNRAS, 391, 268
Gourgouliatos K. N., Vlahakis N., 2010, Geophys. Astrophys. Fluid Dynamics, 104, 431
Harten A., Lax P. D., van Leer B., 1983, SIAM Rev., 25, 35
Hurley K. et al., 2005, Nat, 434, 1098
Keil W., Janka H.-T., Mueller E., 1996, ApJ, 473, L111
Kennel C. F., Coroniti F. V., 1984, ApJ, 283, 710
Low B. C., 1982a, ApJ, 254, 796
Low B. C., 1982b, ApJ, 261, 351
Low B. C., 1984a, ApJ, 281, 392
Low B. C., 1984b, ApJ, 281, 381
Lyutikov M., 2002, Phys. Fluids, 14, 963
Lyutikov M., 2006, MNRAS, 367, 1594
Lyutikov M., Blandford R., 2003, preprint (astro-ph/0312347)
Meliani Z., Sauty C., Vlahakis N., Tsinganos K., Trussoni E., 2006, A&A, 447, 797
Mereghetti S., 2008, A&AR, 15, 225
Mignone A., Bodo G., 2006, MNRAS, 368, 1040
Mobarry C. M., Lovelace R. V. E., 1986, ApJ, 309, 455
Piran T., Shemi A., Narayan R., 1993, MNRAS, 263, 861
Prendergast K. H., 2005, MNRAS, 359, 725
Sari R., 2006, Phys. Fluids, 18, 027106
Shapiro P. R., 1979, ApJ, 233, 831
Spitkovsky A., 2005, in KITP Program: Physics of Astrophysical Outflows and Accretion Discs. Santa Barbara, April 4 – July 29 2005. http://online.kitp.ucsb.edu/online/
Stone J. M., Norman M. L., 1992, ApJS, 80, 753
Stone J. M., Hawley J. F., Evans C. R., Norman M. L., 1992, ApJ, 388, 415
Takahashi H. R., Asano E., Matsumoto R., 2009, MNRAS, 394, 547
Terasawa T. et al., 2005, Nat, 434, 1110
Uchida T., 1997, Phys. Rev. E, 56, 2181
van Leer B., 1977, J. Comput. Phys., 23, 263
Woods P. M., Thompson C., 2006, in Lewin W., van der Klis M., eds, Cambridge Astrophys. Ser. Vol. 39, Compact Stellar X-ray Sources. Cambridge Univ. Press, Cambridge, p. 547
Woods P. M., Kouveliotou C., Göğüş E., Finger M. H., Swank J., Smith D. A., Hurley K., Thompson C., 2001, ApJ, 552, 748

This paper has been typeset from a TEX/LATEX file prepared by the author.